

# Magnetic phase diagrams of barcode-type nanostructures

B. Leighton<sup>1,2</sup>, O. J. Suarez<sup>3</sup>, P. Landeros<sup>3</sup>, and J. Escrig<sup>1,2</sup>

<sup>1</sup> *Departamento de Física, Universidad de Santiago de Chile (USACH),  
Avenida Ecuador 3493, 917-0124 Santiago, Chile*

<sup>2</sup> *Centro para el Desarrollo de la Nanociencia y Nanotecnología, CEDENNA, 917-0124 Santiago, Chile*

<sup>3</sup> *Departamento de Física, Universidad Técnica Federico Santa María,  
Avenida España 1680, Casilla 110 V, 2340000 Valparaíso, Chile*

The magnetic configurations of barcode-type magnetic nanostructures consisting of alternate ferromagnetic and nonmagnetic layers arranged within a multilayer nanotube structure are investigated as a function of their geometry. Based on a continuum approach we have obtained analytical expressions for the energy which lead us to obtain phase diagrams giving the relative stability of characteristic internal magnetic configurations of the barcode-type nanostructures.

PACS numbers: 75.75.+a, 75.10.-b

## I. INTRODUCTION

Magnetic nanoparticles have attracted increasing interest among researchers of various fields due to their promising applications in hard disk drives, magnetic random access memory, and other spintronic devices. [1–5] In addition, these magnetic nanoparticles can be used for potential biomedical applications, such as magnetic resonance imaging (the nanoparticles can be used to trace bioanalytes in the body), cell and DNA separation, and drug delivery. [6] To apply nanoparticles in various potential devices and architectures, it is very important to control their size and shape in order to keep the thermal and chemical stability. [7]

The trusty sphere remains the preferred shape for nanoparticles but this geometry leaves only one surface for modification, complicating the generation of multifunctional particles. Thus, a technology that could modify differentially the inner and outer surfaces would be highly desirable. [8] Tubular nanostructures have stimulated extensive research efforts in recent years because of their particular significance for prospective applications. A wide range of materials including semiconductors, polymers, and metals have been prepared in the form of nanotubes. [9–13] Although the magnetic nanotubes has been intensely investigated, barcode-type nanostructures have received less attention, in spite of tailoring the multisegmented nanotube structure, along with the functionalization of the inner wall surface of barcode-type nanotubes with various molecules (for example, proteins and DNA). Moreover, they are expected to be particularly useful in the field of catalysis, advanced microfluidics, molecule separation and biological and magnetic sensors as well. [14–19] It is worth to mention that barcode-type magnetic nanostructures consisting of regular arrays of magnetic segments have been considered as providing the basis for extending magnetic storage densities beyond the superparamagnetic limit. In such system, a single tube with  $n$  magnetic layers might store up to  $2^n$  bits, whose volume is much larger than those of the grains in conventional recording media,

bearing this way thermal fluctuations and increasing the recording density by a factor  $2^{n-1}$ . [20, 21] Recently, [14] the preparation of metallic nanotubes based on the preferential electrodeposition of a metal along the pore walls of an anodic alumina oxide (AAO) membrane, in the presence of metallic nanoparticles on the wall surfaces, has been reported. In the paper by Lee *et al.* [14] they were able to prepare multisegmented metallic nanotubes with a bimetallic stacking configuration along the tube axis, showing different magnetic behavior as compared with continuous ones, which encourage a study about the possible magnetic configurations and magnetostatic interactions in these barcode-type magnetic nanotubes. Clearly, for the development of magnetic devices based on those arrays, knowledge of the internal magnetic structure of the barcode-type nanostructures is of fundamental importance.

The purpose of this paper is to investigate the magnetic ordering of barcode-type nanostructures. Our particles are characterized by a set of geometrical parameters, as depicted in Fig. 1. First, their external and internal radii,  $R$  and  $a$ , respectively, and total length,  $L$ , which includes the magnetic matter as well as the nonmagnetic one. It is convenient to define the ratio  $\beta \equiv a/R$ , so that  $\beta = 0$  represents a solid cylinder and  $\beta \rightarrow 1$  corresponds to a very narrow tube. We denote with  $W$  the length of each ferromagnetic segment and with  $d$  the length of each nonmagnetic portion, so that, if we have a barcode-type structure with  $n$  magnetic tubes, the total length can be written as  $L = nW + (n + 1)d$ .

## II. MODEL AND DISCUSSION

We adopt a simplified description of the magnetic system in which the discrete distribution of magnetic moments is replaced by a continuous one, defined by the magnetization vector field  $\mathbf{M}(\mathbf{r})$  such that  $\mathbf{M}(\mathbf{r})\delta v$  gives the total magnetic moment within an elementary volume  $\delta v$  centered at  $\mathbf{r}$ . The total magnetic energy ( $E_{tot}$ ) is generally given by the sum of four terms: exchange, dipolar, anisotropy and Zeeman contributions, which are

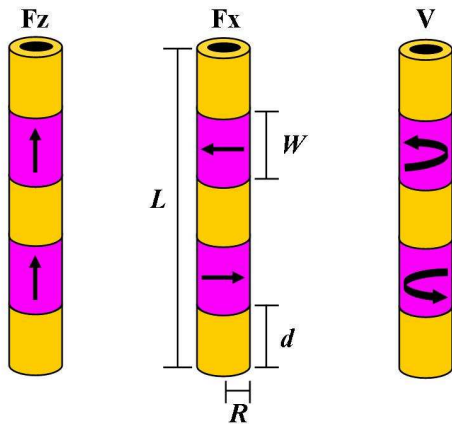


FIG. 1: Geometrical parameters and magnetic configurations of barcode-type nanostructures.

taken from the well known continuum theory of ferromagnetism. [22] As we are interested in the study of the relative stability of the zero-field magnetic ground states, the contribution of the Zeeman energy can be disregarded. Under these assumptions, the magnetic energy is just given by the dipolar ( $E_{dip}$ ), exchange ( $E_{ex}$ ), and anisotropy ( $E_k$ ) contributions.

The total magnetization can be written as  $\mathbf{M}(\mathbf{r}) = \sum_{i=1}^n \mathbf{M}_i(\mathbf{r})$ , where  $\mathbf{M}_i(\mathbf{r})$  is the magnetization of the  $i$ -th ferromagnetic segment. In this case, the magnetostatic potential  $U(\mathbf{r})$  splits up into  $n$  components,  $U_i(\mathbf{r})$ , associated with the magnetization of each ferromagnetic segment. Then, the total dipolar energy can be written as  $E_{dip} = \sum_{i=1}^n E_{dip}(i) + \sum_{i=1}^{n-1} \sum_{j=i+1}^n E_{int}(i, j)$ , where

$$E_{dip}(i) = \frac{\mu_0}{2} \int \mathbf{M}_i(\mathbf{r}) \cdot \nabla U_i(\mathbf{r}) dv,$$

is the dipolar contribution to the self-energy of the  $i$ -th ferromagnetic segment, and

$$E_{int}(i, j) = \mu_0 \int \mathbf{M}_i(\mathbf{r}) \cdot \nabla U_j(\mathbf{r}) dv,$$

is the dipolar interaction between ferromagnetic segments  $i$  and  $j$ .

Usually, the exchange energy  $E_{ex}$  in multilayer nanostructures has contributions from both, the direct exchange interaction within the magnetic segments and the other from the indirect interaction between them mediated by the conduction electrons in the nonmagnetic layers. Since the indirect interaction decays rapidly with the thickness of the nonmagnetic segment, it can be neglected provided  $d$  is large enough. A good estimate of the range of the indirect exchange interaction can be obtained from the results for multilayers. [23] As a general result, the interlayer exchange coupling vanishes for spacer thicknesses greater than a few nanometers, which does not exceed the

value of the exchange length  $l_x = \sqrt{2A/\mu_0 M_0^2}$  of ferromagnetic metals. Here we focus our attention on those cases in which  $d$  is not smaller than the magnetic material's  $l_x$ , as the tubes fabricated by Lee *et al.* [14] which satisfy  $d \gg l_x$  and thus interlayer exchange coupling can be safely neglected. Therefore, to a good approximation can be written as  $E_{ex} = \sum_{i=1}^n E_{ex}(i)$ , where  $E_{ex}(i) = A \int [(\nabla m_{ix})^2 + (\nabla m_{iy})^2 + (\nabla m_{iz})^2] dv$ . Here,  $\mathbf{m}_i = (m_{ix}, m_{iy}, m_{iz}) = \mathbf{M}_i/M_0$  is the magnetization normalized to the saturation magnetization  $M_0$  and  $A$  is the stiffness constant of the magnetic material.

The cubic anisotropy energy of the particle can be added by means of the following expression:

$$E_c(i) = K_c \int (m_{ix}^2 m_{iy}^2 + m_{iy}^2 m_{iz}^2 + m_{iz}^2 m_{ix}^2) dv,$$

and the uniaxial anisotropy energy is given by

$$E_u(i) = -K_u \int m_{iz}^2 dv.$$

On the basis of the above results, the total energy of the barcode-type nanostructure can be written as  $E_{tot} = \sum_{i=1}^n E_{self}(i) + \sum_{i=1}^{n-1} \sum_{j=i+1}^n E_{int}(i, j)$ , where  $E_{self}(i) = E_{dip}(i) + E_{ex}(i) + E_k(i)$  is the self-energy of the ferromagnetic segment  $i$ , and  $E_{int}$  is the (dipolar) interaction energy between two magnetic segments. We will proceed to describe the magnetization of the different states we are considering here and then we will evaluate the magnetic energy of each configuration. Results will be given in units of  $\mu_0 M_0^2 l_x^3$ , i.e.,  $\bar{E} = E/\mu_0 M_0^2 l_x^3$ .

### A. Magnetic configurations

It has been shown recently that single magnetic nanorings present three basic ground states depending on their geometry (see Fig. 1). [24, 25] These configurations are: (Fz) a quasi uniform magnetization state oriented in the direction parallel to the cylindrical axis ( $z$  axis); (Fx) a quasi uniform magnetization state oriented in the plane perpendicular to the  $z$  axis; and (V) a flux-closure vortex state. For long nanorings ( $W \gg R$ ), the Fx phase is not present, [24, 25] a result that holds for nanotubes. [26, 27]

It has been shown for Rothman *et al.* [28] that for magnetized nanorings the single-domain in-plane ground state is the *onion* state. Besides, the single-domain axial state for rings with small inner diameter might be similar to the *flower* state expected in thick axially magnetized cylinders. [29] Therefore, it may appear questionable to select the uniform in-plane and axial as single-domain states to build the phase diagram upon, as they are not stable configurations at a zero applied field. However, it has been verified by micromagnetic simulations [24] and analytical calculations [25] that the energy difference between the actual single-domain ground state in a nanoring, and the uniform state, often turns out to be very

small. From this available evidence, we conclude that the replacement of the more correct quasi-uniform states by simpler ideal uniform states, only results in uncertainties on the exact location of the phase boundaries and on some physical values extracted from the phase diagram.

### 1. Fz state

For the Fz state, where the magnetization of the  $n$  ferromagnetic segments is uniform and parallel to the  $z$  axis,  $\mathbf{M}(\mathbf{r})$  can be approximated by  $M_0\hat{z}$ , where  $\hat{z}$  is the unit vector parallel to the axis of the nanotube. In this case the exchange contribution to the self energy vanishes, and the reduced self energy takes the form [26]

$$\tilde{E}_{self}^{Fz} = \frac{\pi R^3}{l_x^3} \int_0^\infty \frac{dq}{q^2} \left(1 - e^{-q\frac{W}{R}}\right) (J_1(q) - \beta J_1(q\beta))^2 - \frac{\kappa_u \pi W R^2}{2 l_x^3} (1 - \beta^2),$$

where  $J_1(z)$  is a Bessel function of the first kind and  $\kappa_u = 2K_u/\mu_0 M_0^2$ . In order to calculate the interaction energy between the ferromagnetic segments, we first need to calculate the magnetostatic potential  $U(\mathbf{r})$  of a single tubular structure. The expression for this potential has been previously reported [30] and is given by

$$U(r, z) = \frac{M_0}{2} \int_0^\infty \frac{dk}{k} J_0(kr) [R J_1(kR) - a J_1(ka)] \left( e^{-k|\frac{W}{2}-z|} - e^{-k|\frac{W}{2}+z|} \right).$$

From this equation it is possible to obtain the expression for the magnetostatic field. Thus we write,  $\mathbf{H}(r, z) = -\nabla U(r, z) = H_r(r, z)\hat{r} + H_z(r, z)\hat{z}$  with

$$H_r(r, z) = \frac{M_0}{2} \int_0^\infty dk J_1(kr) [R J_1(kR) - a J_1(ka)] \left( -e^{-k|\frac{W}{2}-z|} + e^{-k|\frac{W}{2}+z|} \right)$$

and

$$H_z(r, z) = \frac{M_0}{2} \int_0^\infty dk J_0(kr) [R J_1(kR) - a J_1(ka)] Y(W, z)$$

where  $Y(W, z) = \text{sign}\left(\frac{W}{2} - z\right) e^{-k|\frac{W}{2}-z|} - \text{sign}\left(-\frac{W}{2} - z\right) e^{-k|\frac{W}{2}+z|}$ . The function  $\text{sign}(x)$  gives  $-1$ ,  $0$  or  $1$  depending on whether  $x$  is negative, zero, or positive. Figure 2 illustrates the magnetostatic field profile calculated analytically for nanotubes with the same geometrical parameters as the ones investigated experimentally by Lee *et al.* [14]. Finally, the reduced interaction energy between two tubular nanostructures has been calculated in rather general way by Escrig *et*

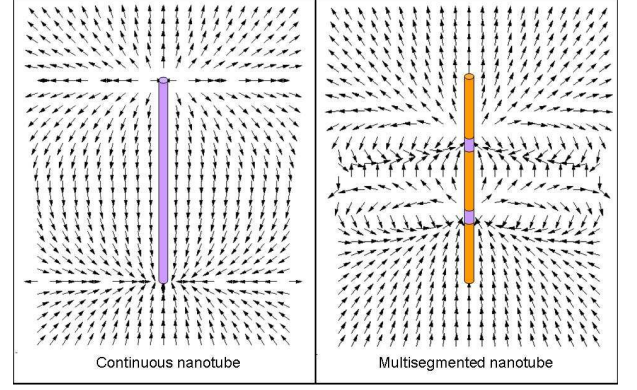


FIG. 2: Stray field direction (arrows) generated by a single nanotube (*left picture*) and a multisegmented nanotube (*right picture*) magnetized in the  $+z$  direction. These two examples correspond to nanotubes with the same geometrical parameters as those studied experimentally by Lee *et al.* [14].

*al.* [21, 30] and is given by

$$\tilde{E}_{int}^{Fz}[d] = -\frac{\pi R^3}{l_x^3} \int_0^\infty \frac{dq}{q^2} e^{-q\frac{d}{R}} \left(1 - e^{-q\frac{W}{R}}\right)^2 (J_1(q) - \beta J_1(q\beta))^2.$$

Thus, the reduced total energy for the Fz state can be expressed as

$$\tilde{E}_{tot}^{Fz} = n\tilde{E}_{self}^{Fz} - \frac{\pi R^3}{l_x^3} \int_0^\infty \frac{dq}{q^2} e^{-q\frac{W}{R}} \left(1 - e^{-q\frac{W}{R}}\right) (J_1(q) - \beta J_1(q\beta))^2 g_z(n, q, \sigma),$$

where  $g_z(n, q, \sigma) = \frac{(n-1)e^{q\sigma} + e^{-(n-1)q\sigma} - n}{(1-e^{q\sigma})^2}$  and  $\sigma = \frac{d+W}{R}$ .

### 2. Fx state

For the Fx state,  $\mathbf{M}(\mathbf{r})$  can be generally considered as  $M_0 \cos[(i-1)\theta]\hat{x} + M_0 \sin[(i-1)\theta]\hat{y}$ , which represent a helicoidal magnetic state, with  $\theta$  the angle between the in-plane magnetization of adjacent segments. For the in-plane state, the exchange and anisotropy contributions to the self energy vanish and the reduced self energy takes the form [21]

$$\tilde{E}_{self}^{Fx} = \frac{\pi R^3}{2l_x^3} \int_0^\infty \frac{dq}{q^2} \left( e^{-q\frac{W}{R}} + q\frac{W}{R} - 1 \right) (J_1(q) - \beta J_1(q\beta))^2,$$

where  $J_1(z)$  is a Bessel function of the first kind. In order to calculate the interaction energy between the ferromagnetic segments, we first need to calculate the magnetostatic potential  $U(\mathbf{r})$  of a single tubular structure. The

expression for this potential is given by

$$U(r, \phi, z) = M_0 \cos \phi \int_0^\infty \frac{dk}{k} J_1(kr) f(k) \begin{cases} e^{-kz} \sinh\left(k\frac{W}{2}\right) & z > \frac{W}{2} \\ \left(1 - e^{-k\frac{W}{2}} \cosh(kz)\right) & -\frac{W}{2} < z < \frac{W}{2} \\ e^{kz} \sinh\left(k\frac{W}{2}\right) & z < -\frac{W}{2} \end{cases},$$

where  $f(k) = (RJ_1(kR) - aJ_1(ka))$ . Finally, the reduced interaction energy between two tubular nanostructures is given by

$$\tilde{E}_{int}^{Fx} [d, \theta] = \frac{\pi R^3}{2l_x^3} \cos \theta \int_0^\infty \frac{dq}{q^2} e^{-q\frac{d}{R}} \left(1 - e^{-q\frac{W}{R}}\right)^2 (J_1(q) - \beta J_1(q\beta))^2.$$

Thus, the reduced total energy for the Fx state can be expressed as

$$\tilde{E}_{tot}^{Fx} = n\tilde{E}_{self}^{Fx} + \frac{\pi R^3}{2l_x^3} \int_0^\infty \frac{dq}{q^2} e^{q\frac{W}{R}} \left(1 - e^{-q\frac{W}{R}}\right)^2 (J_1(q) - \beta J_1(q\beta))^2 g_x(n, q, \sigma, \theta),$$

where  $g_x(n, q, \sigma, \theta) = \sum_{i=1}^{n-1} \sum_{j=i+1}^n e^{-q\sigma(j-i)} \cos[(j-i)\theta]$  and  $\sigma = \frac{d+W}{R}$ . From this expression we can conclude that for zero applied field the total energy of this state is further reduced for the value  $\theta = \pi$ , independently of the value of  $n$ . Thus, for the particular case when  $\theta = \pi$  we obtain  $g_x(n, q, \sigma, \pi) = -\frac{e^{q\sigma(1-n)}[(-1)^n - e^{nq\sigma}] + (1 + e^{q\sigma})n}{(1 + e^{q\sigma})^2}$ .

### 3. Vortex state

Finally, for the vortex state V,  $\mathbf{M}(\mathbf{r})$  can be approximated by  $M_0\hat{\phi}$ , where  $\hat{\phi}$  is the azimuthal unit vector. Due to the condition of perfect flux closure in the vortex configuration, one magnetic nanostructure in such configuration does not interact with others, independently of the magnetic configuration of those. Thus, there is no difference between clockwise and counter-clockwise directions. Finally, the reduced total energy for the vortex state is given just by the  $n$  self energies [21, 26]

$$\tilde{E}^V = -n\frac{\pi W \ln \beta}{l_x} + n\frac{\kappa_c}{16} \frac{\pi W R^2}{l_x^3} (1 - \beta^2).$$

Here,  $\kappa_c = 2K_c/\mu_0 M_0^2$ .

### B. Phase diagram for multisegmented nanorings

We proceed to investigate the relative stability of the configurations. Phase diagrams are shown in Fig. 3 for  $d = l_x$ ,  $\beta = 0.5$ , and  $n = 5$ . Anisotropy for four different materials are considered according to values presented in

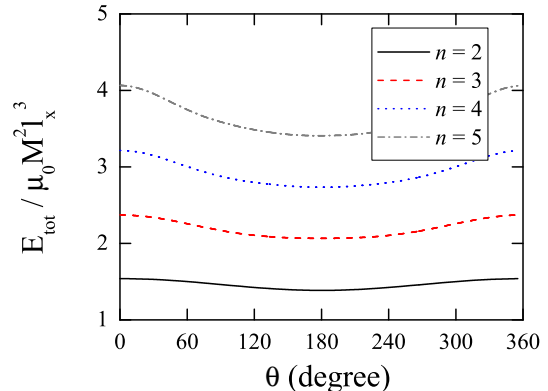


FIG. 3: Phase diagrams for barcode-type nanostructures giving the regions in the RW plane where one of the configurations has lower energy. We have used  $\beta = 0.5$ ,  $d = l_x$ , and  $n = 5$ .

TABLE I: Parameters for different materials taken from Ref. [31]. Uniaxial ( $K_u$ ) cobalt is denoted with a superscript \*. Iron, permalloy and nickel have cubic ( $K_c$ ) anisotropy.

Material	$K$ (J/m <sup>3</sup> )	$\kappa$
Iron	$4.8 \times 10^4$	0.0264
Cobalt*	$4.1 \times 10^5$	0.3329
Permalloy	$-3.0 \times 10^2$	-0.0007
Nickel	$-4.5 \times 10^3$	-0.0304

Table 1. The diagrams show three regions, corresponding to configurations Fz, Fx, and V, as in the case of a single nanoring ( $n = 1$ ). Notice that for the case of Co, the existence of a strong uniaxial anisotropy favors the Fz phase, decreasing the other two phases, specially the V one. In the case of a cubic anisotropy, the transition lines are similar to the case of a phase diagram without anisotropy. Because of its very low anisotropy, results for permalloy describe reasonably well a material with no anisotropy, as it was pointed in Ref. [27].

Since nanostructures are usually polycrystalline, the crystallographic orientations of the crystallites are random and, as a consequence, the average magnetic anisotropy of the particle is very small. In view of that, it will be neglected in our calculations. [32, 33]

For different values of  $n$  we can determine the ranges of values of the dimensionless radius  $R/l_x$  and length  $W/l_x$  within which one of the three configurations is of lowest energy. The boundary line between any two configurations can be obtained by equating the expressions for the corresponding total energies. Figure 4 illustrates phase diagrams for  $d = l_x$ ,  $\beta = 0.5$ , and  $n = 1$  (solid lines), 3 (dotted lines), and 5 (dashed lines). It is important to ob-

serve that for the Fz and Fx states the exchange energy is the same. Then, in the absence of applied magnetic fields and crystalline anisotropies, the dipolar energy is fundamental to obtain the magnetic configuration of lowest energy. Thus, the dipolar contribution represents the shape anisotropy that, for multisegmented nanostructures with a small length (namely nanorings) the low energy state is the quasi uniform in-plane configuration Fx. [25] As the length is increased, but keeping the radius small enough, there is a transition to the out-of-plane state Fz at a critical length whose value depends on  $R$ ,  $\beta$ , and the exchange length  $l_x$ . As the radius is increased, the magnetizations turns to the vortex configuration at a critical radius depending on the values of  $W$ ,  $\beta$ , and  $l_x$ . Finally, by comparing our results we observe differences in the behavior of the triple point as a function of  $n$ . The triple point occurs for smaller  $R/l_x$  when  $n$  is decreased.

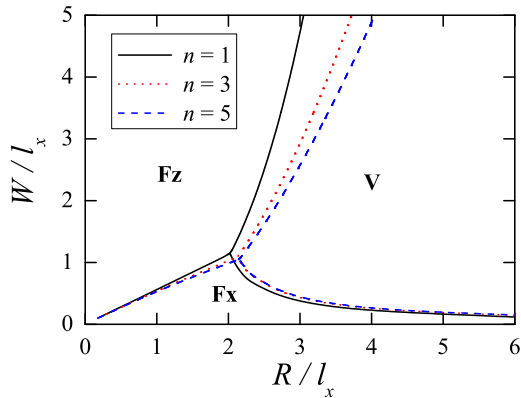


FIG. 4: Phase diagrams for barcode-type nanostructures with  $\beta = 0.5$  and  $d = l_x$ .

Similar to the case of a single ring, the phase diagram changes with  $\beta$  [25]. The dependence of the whole diagram on the value of  $n$  can be investigated by looking at the trajectories of the triple point in the  $RW$  plane as functions of  $\beta$ . Such trajectories are shown in Fig. 5 for  $d = l_x$  and different values of  $n$ . We remark that the radius  $R_t$  of the triple point represents the smallest value of  $R$  for which the vortex configurations are stable, and  $W_t$  is the biggest value of  $W$  for which the in-plane configurations are stable.

### C. Phase diagram for multisegmented nanotubes

As the multisegmented tubes that motivate this work [14] satisfy  $W/R \gg 1$ , then the Fx phase can be left out of consideration. Thus, to obtain an expression for the transition line separating the Fz phase from the V phase we match the expressions for the energy of these two configurations. It is important to mention that, for

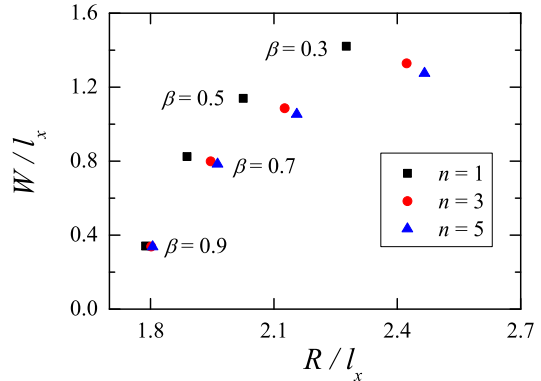


FIG. 5: Trajectories of the triple point in the phase diagrams in Fig. 4 as functions of  $\beta$ , for  $n = 1$  (squares), 3 (circles), and 5 (triangles).

tubes with long radius, it has been observed a third state which is a mixture of the other two and has been called *bamboo* or *mixed* state. [34–37] As it is known, the consideration of no uniform magnetic configurations complicates considerably the calculations and for simplicity, we studied multisegment magnetic nanotubes whose radius are not big enough to allow the formation of relevant vortex domains at the extremes of the tube. Figure 6 presents the transition line for  $n = 1$  and  $n = 2$ . To the left of each line Fz state prevails while to the right of the same line the vortex V configuration is more stable. Labelled dots (*continuous*) and (*multisegmented*) in Fig. 6 correspond to the cases of the two hysteresis curves reported in the experimental paper by Lee *et al.* [14] defined by (*continuous*)  $n = 1$ ,  $R = 150$  nm,  $W = 16$   $\mu\text{m}$ ,  $\beta = 0.75$ , and  $l_x = 8.225$  nm; (*multisegmented*)  $n = 2$ ,  $R = 150$  nm,  $W = 800$  nm,  $d = 4800$  nm,  $\beta = 0.75$ , and  $l_x = 8.225$  nm. It is important to note that the transition line for  $n = 1$  is almost equal to the one with  $n = 2$ . It is due to that average distance between the neighboring Ni segments was big enough ( $d = 4.8$   $\mu\text{m}$ ) avoiding thus the interaction between the segments. From this figure we can conclude that the multisegmented system is well inside the V phase while the continuous system is inside the Fz phase. It allows us to understand why the experimental samples show a different magnetic behavior; simply they have substantial differences in their length of the ferromagnetic segments.

The results presented above may be generalized. We now proceed to investigate the transition line separating the Fz phase from the V phase. To obtain an expression for this transition line we match the expressions for the energy of these two configurations. This leads to  $W/l_x = \alpha(\beta) \times R^3/l_x^3$ . Function  $\alpha(\beta)$  is plotted in Fig. 7. Care must be applied in the limits of the intervals for  $\beta$ . In particular, when  $\beta$  goes to 1 we deal with ex-

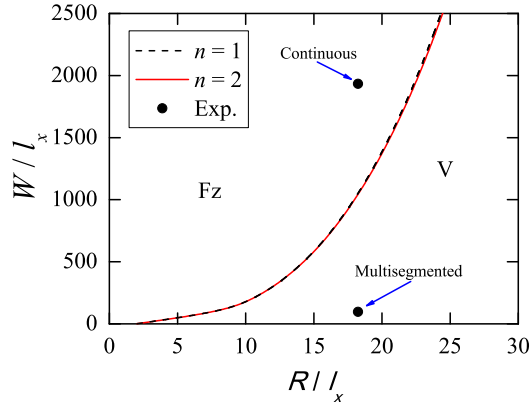


FIG. 6: Magnetic phase diagrams of non-interacting multisegmented nanotubes for different values of  $n$ . The dimensions of the tube,  $W$  and  $R$ , are normalized to the exchange length  $l_x$ . Experimental points are discussed in the text.

tremely narrow nanotubes, where eventual surface roughness and thickness irregularities of the nanotubes become important. On the other side, when  $\beta$  goes to zero we are approaching the limit of a solid cylinder, where the core in the vortex phase becomes important and must be considered to get the solution. As the multisegmented nanotubes considered experimentally have  $\beta \approx 0.75$ , we have neglected these two cases.

### III. CONCLUSIONS

In conclusion, we have studied the relative stability of ideal configurations of magnetic barcode-type tubular nanostructures composed of alternate ferromagnetic and non-magnetic layers. In such systems we investigated the size range of the geometric parameters for which different configurations are of lowest energy. Results are summarized in phase diagrams which clearly indicate that the magnetic behavior of such structures can be tailored to meet specific requirements provide a judicious choice of such parameters is made. The lines separating the magnetic phases and, in particular, the triple point, are very sensitive to the geometry of the barcode-type nanostructures. The phase diagrams presented can provide guide-

lines for the production of nanostructures with technological purpose.

### IV. ACKNOWLEDGMENTS

We thank D. Altbir and K. Nielsch for useful discussions. This work was partially supported by FONDECYT grant numbers 11070010 and 11080246, Financiamiento Basal para Centros Científicos y Tecnológi-

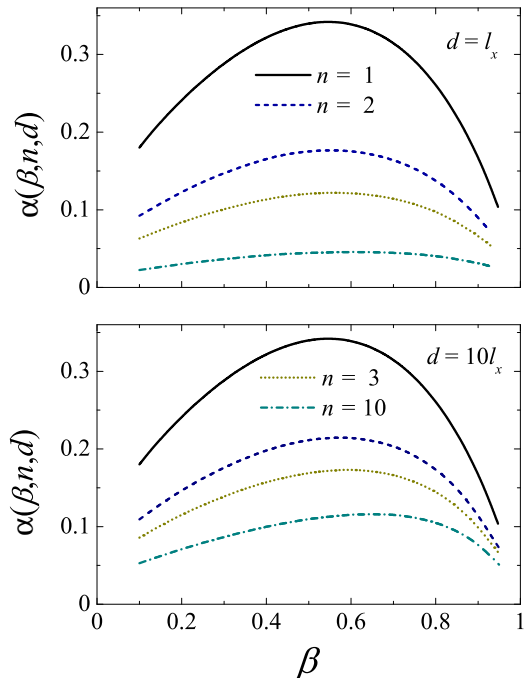


FIG. 7: Function  $\alpha(\beta)$  defining the transition condition from the phase diagram of a multisegmented nanotube.

cos de Excelencia, Millennium Science Initiative under Project P06-022-F, the program “Bicentenario en Ciencia y Tecnología” PBCT under project PSD-031 and the internal Grant USM-DGIP 11.08.57. We also acknowledge support from the grant program AGCI, CONICYT, and the program PIIC2009 USM (Chile).

[1] Sun S, Murray C B, Weller D, Folks L and Moser A 2000 *Science* **287** 1989.

[2] Koch R H, Deak J G, Abraham D W, Trouilloud P L, Altman R A, Lu Yu, Gallagher W J, Scheuerlein R E, Roche K P and Parkin S S P 1998 *Phys. Rev. Lett.* **81**, 4512.

[3] Cowburn R P, Koltsov D K, Adeyeye A O, Welland M E and Tricker D M 1999 *Phys. Rev. Lett.* **83**, 1042.

[4] Wolf S A, Awschalom D D, Buhrman R A, Daughton J M, von Molnar S, Roukes M L, Chtchelkanova A Y and Treger M 2001 *Science* **294**, 1488.

[5] Gerrits Th, van den Berg H A M, Hohlfield J, Bar L and

- Rasing Th 2002 *Nature (London)* **418**, 509.
- [6] Emerich D F and Thanos C G 2003 *Expert Opin. Biol. Ther.* **3**, 655.
- [7] Puentes V F, Krishnan K M and Alivisatos A P 2001 *Science* **291**, 2115.
- [8] Eisenstein M 2005 *Nat. Methods* **2**, 484.
- [9] Yanagishita T, Sasaki M, Nishio K and Masuda H 2004 *Adv. Mater.* **16**, 429.
- [10] Wu G, Zhang L, Cheng B, Xie T and Yuan X 2004 *J. Am. Chem. Soc.* **126**, 5976.
- [11] Mu C, Yu Y, Wang R, Wu K, Xu D and Guo G 2004 *Adv. Mater.* **16**, 1550.
- [12] Bachmann J, Jing J, Knez M, Barth S, Shen H, Mathur S, Gosele U and Nielsch K 2007 *J. Am. Chem. Soc.* **129**, 9554.
- [13] Escrig J, Bachmann J, Jing J, Daub M, Altbir D and Nielsch K 2008 *Phys. Rev. B* **77**, 214421.
- [14] Lee W, Scholz R, Nielsch K and Gosele U 2005 *Angew. Chem. Int. Ed.* **44**, 6050.
- [15] Nicewarner-Pena Sheila R, Griffith Freeman R, Reiss Brian D, He Lin, Pena David J, Walton Ian D, Cromer Remy, Keating Christine D and Natan Michael J 2001 *Science* **294**, 137.
- [16] Lehmann Volker 2002 *Nature Materials* **1**, 12.
- [17] Nicewarner-Pena Sheila R, Carado Anthony J, Shale Kristen E and Keating Christine D 2003 *J. Phys. Chem. B* **107**, 7360.
- [18] Stoermer Rebecca L, Cederquist Kristin B, McFarland Sean K, Sha Michael Y, Penn Sharron G and Keating Christine D 2006 *J. Am. Chem. Soc.* **128**, 16892.
- [19] Son Sang Jun, Reichel Jonathan, He Bo, Schuchman Mattan, Lee Sang Bok 2005 *J. Am. Chem. Soc.* **127**, 7316-7317.
- [20] Albrecht M, Hu G, Moser A, Hellwig O and Terris B D 2005 *J. Appl. Phys.* **97**, 103910.
- [21] Escrig J, Landeros P, Altbir D, Bahiana M and d'Albuquerque e Castro J 2006 *Appl. Phys. Lett.* **89**, 132501.
- [22] Aharoni A 1996 *Introduction to the Theory of Ferromagnetism* (Clarendon, Oxford) Chapter 7.
- [23] See, for example, Bloemen P J, Johnson M T, van de Vorst M T H, Coehoorn R, de Vries J J, Jungblut R, van de Stegge J, Reinders A and de Jonge W J M 1994 *Phys. Rev. Lett.* **72**, 764.
- [24] Beleggia M, Lau J W, Schofield M A, Zhu Y, Tandon S and De Graef M 2006 *J. Magn. Magn. Mater.* **301**, 131-146.
- [25] Landeros P, Escrig J, Altbir D, Bahiana M and d Albuquerque e Castro J 2006 *J. Appl. Phys.* **100**, 044311.
- [26] Escrig J, Landeros P, Altbir D, Vogel E E and Vargas P 2007 *J. Magn. Magn. Mater.* **308**, 233-237.
- [27] Escrig J, Landeros P, Altbir D and Vogel E E 2007 *J. Magn. Magn. Mater.* **310**, 2448-2450.
- [28] Rothman J, Klaui M, Lopez-Diaz L, Vaz C A F, Bleloch A, Bland J A C, Cui Z and Speaks R 2001 *Phys. Rev. Lett.* **86**, 1098.
- [29] Usov N A and Peschany S E 2004 *J. Magn. Magn. Mater.* **130**, 275.
- [30] Escrig J, Allende S, Altbir D and Bahiana M 2008 *Appl. Phys. Lett.* **93**, 023101.
- [31] O'Handley R C 2000 *Modern Magnetic Materials* (Wiley, New York, USA).
- [32] Klaui M, Vaz C A F, Lopez-Diaz L and Bland J A C 2003 *J. Phys.: Condens. Matter* **15**, R985.
- [33] Castaño F J, Ross C A, Eilez A, Jung W and Frandsen C 2000 *Phys. Rev. B* **69**, 144421.
- [34] Wang Z K *et al* 2005 *Phys. Rev. Lett.* **94**, 137208.
- [35] Landeros P, Suarez O J, Cuchillo A and Vargas P 2009 *Phys. Rev. B* **79**, 024404.
- [36] Lee S, Suess D, Schreffl T, Oh K H, Fidler J 2007 *J. Magn. Magn. Mater.* **310**, 2445.
- [37] Chen A P, Usov N A, Blanco J M, Gonzalez J 2007 *J. Magn. Magn. Mater.* **316**, e317.